Irregular Microdome Structure-Based Sensitive Pressure Sensor Using Internal Popping of Microspheres

Young Jung, Jungrak Choi, Wookjin Lee, Jong Soo Ko, Inkyu Park,* and Hanchul Cho*

Modifying the surface morphology of an elastomer surface into 3D micro-structures is crucial for various soft sensor applications. However, processes based on typical mold microfabrication and elastomer casting remain the dominant methodologies. This study demonstrates a novel strategy for generating 3D and irregular microdome structures for flexible pressure sensors through the internal popping of microspheres. When thermal treatment is applied to a composite film composed of microspheres and an elastomer matrix, the microspheres expand, and irregular microdome structures are generated. This composite film with an irregular microdome structure is utilized as a piezoresistive pressure-sensing film. The sensor shows high sensitivity (-50.45 kPa^{-1}) owing to the heterogeneous contact change between the irregular microdome structure and a laser-induced graphene electrode; it also exhibits a short response time ($\tau_{10\text{-}90\%} \approx 39$ ms), excellent repeatability, and high reliability. The sensor is applied in a fingertip-shaped pressure sensor to detect the blood pulse on the index finger and on electronic skin to recognize soft objects. Furthermore, a pressure sensor array that enables various functions such as drawing, multitouch, and deep learning-based motion control, is demonstrated.

1. Introduction

The development of flexible pressure sensors has attracted significant attention owing to their various potential applications in wearable devices,[1] human–machine interfaces,[2,3] and

Y. Jung, J. Choi, I. Park
Department of Mechanical Engineering
Korean Advanced Institute of Science and Technology (KAIST)
Daejeon 34141, Republic of Korea
E-mail: inkyu@kaist.ac.kr
W. Lee
School of Materials Science and Engineering
Pusan National University
Busan 46241, Republic of Korea
J. S. Ko
School of Mechanical Engineering
Pusan National University
Busan 46241, Republic of Korea
H. Cho
Precision Mechanical Process and Control R&D Group
Korea Institute of Industrial Technology (KITECH)
Busan 46938, Republic of Korea
E-mail: hc.cho@kitech.re.kr

health monitoring systems.[4–6] For many of these applications involving low pressure detection such as wrist pulse or soft touch (0–10 kPa), high sensitivity in the low-pressure range are required. Pressure sensing mechanisms can be divided into piezoresistive,[7–12] piezocapacitive,[13–17] piezoelectric,[18,19] or piezotransmittance[20–22] types. Piezoresistive flexible pressure sensors convert physical stimuli into a change in electrical resistance by changing the contact area and pressure between electrodes and sensor structures. This is the most widely used type of soft pressure sensor, since it has the advantages of easy operation, high sensitivity in the low-pressure range, simple structure, and fast response.

An effective approach for fabricating a piezoresistive soft pressure sensor structure with high sensitivity in the low-pressure range is to construct microstructures such as pyramids,[10,12,14,16,23] domes,[8,24–26] and pillars.[27–29] When a physical force is applied to the sensor structure with micro/nanoscale 3D surface morphology, localized stress concentration occurs, inducing a large local strain. Therefore, the sensitivity of the sensor increases in the low-pressure range, and even subtle physical forces can be detected and distinguished. Sensor structures with 3D surface morphology exhibit desirable sensing characteristics, including sensitivity, response time, and limit of detection (LOD). These approaches can be used to manufacture various types of microstructures for high-sensitivity pressure sensor applications.

In general, an effective approach for fabricating a sensor structure with micro/nano-scale 3D surface morphology is the microfabrication of molds and elastomer casting processes. The mold fabrication methods can be divided into the following categories: i) top-down approaches, such as photolithography and silicon etching, and ii) bottom-up approaches using self-assembled particles. For example, Peng et al. fabricated a piezoresistive-based flexible pressure sensor based on conductive polydimethylsiloxane (PDMS) thin films generated by the soft lithography replication of 3D printed templates.[30] The fabricated sensor exhibited a high sensitivity of $\approx$3.6 kPa^{-1}. The authors showed that the sensor could detect a subtle pressure of $\approx$1 Pa. Zhang et al. proposed microstructures using a self-assembled monolayer as a sacrificial template.[31] The fabricated sensor showed a high sensitivity of $\approx$15 kPa^{-1} in a pressure range of 100 Pa or less and could detect a subtle pressure of

≈4 Pa. Although these researches showed that flexible pressure sensors with high sensing performance could be fabricated via conventional microfabrication of molds and elastomer casting, there is still a limitation in fabricating sensor structures with large-scale 3D surface morphology and sensitivity. First, geometrical parameters such as space and size of microstructures should be controlled to enhance the sensing performance. However, abovementioned methods require several iterative processes to fabricate molds such as photolithography and etching, which have low degrees of freedom in the fabrication perspectives. In addition, since regular 3D microstructures are simultaneously deformed together under the pressure and quickly saturated, there is a limitation to improve the sensor sensitivity. Therefore, a novel approach for controlling 3D surface morphology with high degrees of freedom in the fabrication process and well-designed irregular 3D microstructures is needed to achieve the fabrication of the highly sensitive pressure sensor.

In this paper, we propose a novel approach to fabricate a sensor structure with a microscale 3D surface morphology via the internal popping of thermally expandable microspheres. When a thermal treatment is applied to a composite film composed of microspheres and an elastomer matrix, the microspheres expand, and irregular microdome structures are generated. This method allows not only controllable microscale 3D surface morphology via high degrees of freedom in the fabrication process but also highly sensitive pressure sensor owing to the irregular microdome structures. This composite film with an irregular microdome structure coated with a conductive metal layer is used as the top active layer, and laser-induced graphene (LIG) acts as the bottom electrode for pressure sensing. Furthermore, finite-element method (FEM) simulations are employed to understand the compressive behavior of irregular microdome structures as a function of the pressure. We evaluate the sensing performance during static (I–V curves, LOD) and dynamic (reliability, response time, and repeatability) loading, including the sensitivity of the pressure sensors. To demonstrate the potential applications in electronic skin, a fingertip-shaped pressure sensor was developed to detect the blood pulse on the index finger and recognize soft objects. Finally, we demonstrated that large-area and multipixel sensor array pads could realize various functions, such as drawing, multitouch, and deep learning-based motion controllers.

2. Results and Discussion

2.1. Surface Morphology Control via Internal Popping of Thermally Expandable Microspheres

The mechanism of 3D surface morphology control using the internal popping of thermally expandable microspheres is illustrated in **Figure 1**. The microspheres consist of thermoplastic resins (acrylonitrile (AN) copolymers) at the outer shell and liquid hydrocarbon (isopentane) at the inside core (Figure 1a). When a specific temperature is applied to the microspheres, the AN copolymer shell becomes soft (state 1), and the hydrocarbon at the inside core undergoes a phase change from liquid to gas (state 2), gasified hydrocarbon starts to permeate through

thin outer shell to diffuse into the composites. The volume expansion of the microspheres results by three to six times (Video S1, Supporting Information). Figure 1b shows the field-emission scanning electron microscopy (FE-SEM) images and particle diameter distribution before (noted as "initial state") and after (noted as "expansion state") the expansion of microspheres at 170 °C. The FE-SEM images of the four steps of microsphere expansion are shown in Figure S1 of the Supporting Information: at room temperature (RT), at 150 °C where the expansion begins, at 170 °C where the maximum expansion occurs, and finally at 200 °C where the microspheres are shrunken. A histogram and average diameter were obtained by measuring 100 samples after expansion at different temperatures (Table S1 and Figure S2, Supporting Information). At the initial state, the average diameter of the microspheres was measured as 8.49 ± 0.53 μm. There was no significant change in diameter at 140 °C. Some microspheres began to expand at 150 °C, and the average diameter rapidly increased with the heating temperature (e.g., average diameter of 41.35 μm at 170 °C). The inside of microsphere exhibits a rough surface and thickness of shell was measured as ≈1 μm (Figure S3, Supporting Information). However, as the temperature increased above 170 °C, the microspheres shrank due to polymer degradation occurring at the melting temperature, and the overall diameter gradually decreased.

Figure 1c shows a schematic of the 3D surface morphology formation on an elastomer surface using microsphere expansion. Commercial microspheres were mixed with liquid PDMS, in which the resin and hardener were mixed in a 10:1 weight ratio. The PDMS/microsphere precursor was spin-coated on the PI substrate at 1000 rpm for 30 s and then cured at 80 °C for 4 h. The fabricated composite film of microspheres and elastomer exhibits a smooth surface before expansion. Then, irregular microdome structures are generated throughout the surface when heat is applied to the composite film (Video S2, Supporting Information). The formation mechanism of the 3D and irregular microdome structure is explained by the pressure difference between the microspheres and the composite matrix (Figure 1c). In the initial state (Figure 1c(i)), there is no significant change in the surface of the composite film. When a specific temperature is applied to the composite film, the expansion of the microspheres begins due to the increased pressure. The high pressure within the microspheres causes their expansion, forming irregular microdome structures on the surface (Figure 1c(ii)). The microspheres expand until their pressures are in equilibrium with that of the surrounding composite film, resulting in a final 3D surface morphology (Figure 1c(iii)). Figure 1d,e shows the top and cross-sectional FE-SEM images of the fabricated composite film before and after microsphere expansion. Before microsphere expansion, the composite film exhibited a smooth surface with no irregular microdome structures. When microspheres were expanded, irregular microdome structures were randomly and densely formed on the composite surface. The 3D profiles of irregular microdome structures were measured using a confocal laser scanning microscope to observe the changes in morphology by microsphere expansion (Figure 1f). The inset graphs show the cross-sectional profiles along specific lines (AA′ and BB′). Before microsphere expansion, the maximum height on the composite film was measured as only 0.41 μm. By contrast, the
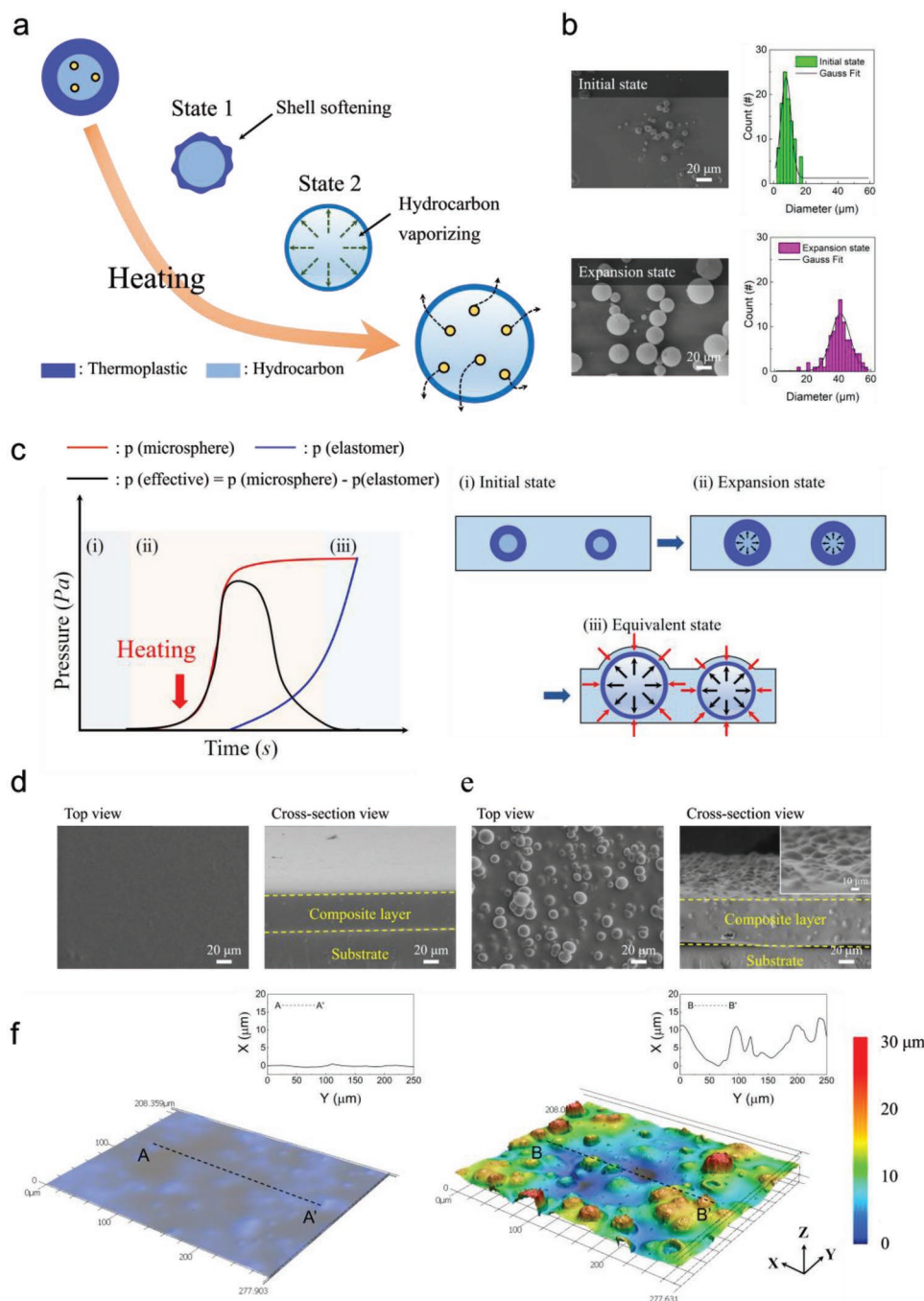
Figure 1. Concept of 3D surface morphology formation using thermal expansion of microspheres. a) Thermal expansion mechanism of microspheres. The AN copolymer shell becomes soft (state 1) and hydrocarbon at the inner core undergoes a phase change from liquid to gas (state 2) by applied temperature. b) FE-SEM images and particle diameter distribution before and after the expansion of microspheres. c) Schematic of 3D surface morphology on an elastomer surface using internal popping of microspheres. d,e) Top and cross-sectional FE-SEM images of the fabricated composite film before (d) and after (e) microsphere expansion. f) 3D profile measurement results of the composite films before (left) and after (right) microsphere expansion.

composite film after microsphere expansion exhibited a maximum height of 13.41 µm. To demonstrate that the microscale 3D surface morphology can be controlled, composite films with different microsphere concentrations (1–9 wt%) were compared (Figure S4, Supporting Information, for details of area fraction). The area fraction of the composite film increased from 4.33% to 56.92% when the microsphere concentration raised from 1 to 9 wt%. The uniformity of the suggested composite film with irregular microdome structures was evaluated with respect to the arithmetic mean height at various points (Figure S5, Supporting Information, for the details of the arithmetic mean height). From the results, the 3D surface morphology can be controlled with high scalability and uniformity according to the microsphere concentration.
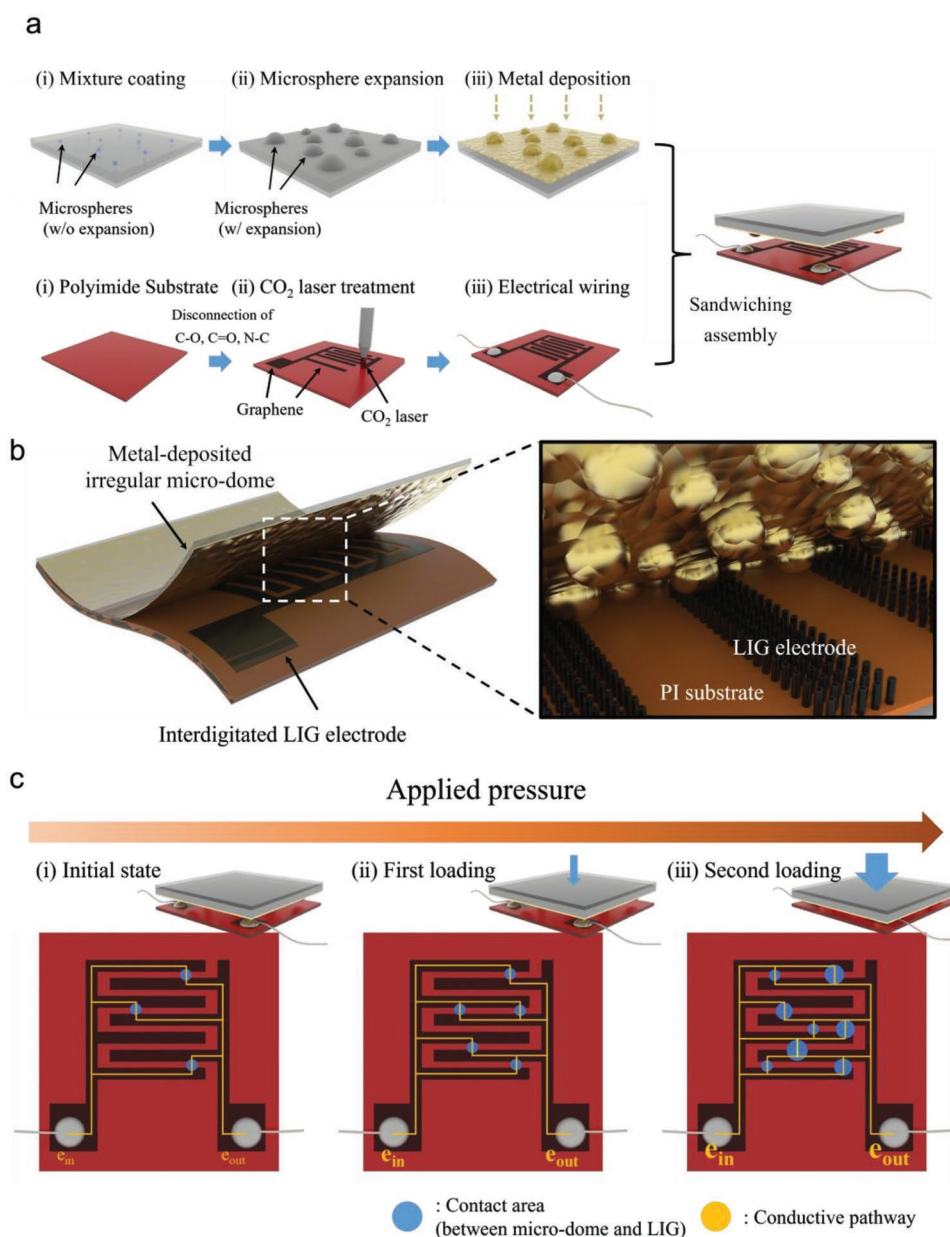
**ADVANCED
SCIENCE NEWS**

www.advancedsciencenews.com

**ADVANCED
FUNCTIONAL
MATERIALS**

www.afm-journal.de

Figure 2. Fabrication procedure for the sensor structure and sensing mechanism. a) Fabrication method of the metal-deposited composite film with irregular microdome structure and interdigitated electrode using laser-induced graphene (LIG). b) Schematic illustration of the pressure sensor with metal-deposited composite film with irregular microdome structure on the top active layer and interdigitated LIG on the bottom sensing electrode. c) Sensing mechanism of the fabricated pressure sensor.

2.2. Fabrication Process and Structure of Flexible Pressure Sensor

The fabrication process of the sensor structure is shown in **Figure 2**a. The top electrode was fabricated by coating a liquid mixture of microspheres and PDMS prepolymer, heating the cured composite film to form a microdome structure, and depositing a thin metal film as a conductive layer. The bottom electrode was fabricated by applying a CO_2 laser on a cleaned polyimide (PI) substrate and connecting this electrode with a copper wire using silver epoxy. The surface of the PI film was irradiated by a CO_2 laser and locally heated at ≈2500 °C via the photothermal effect, which breaks the C−O, C=O, and N−C bonds, and generates C−C bonds in the chemical structures of the PI film.[32] The oxygen and nitrogen components are significantly reduced, and the sp^3 bonds of carbon are converted into sp^2 bonds to produce a high-purity graphene. Energy-dispersive X-ray spectroscopy was used to compare the composition of the PI substrate and LIG layer (Figure S6, Supporting Information). The ratio of carbon and oxygen was changed by varying the CO_2 laser irradiation treatment on the PI substrate, and the carbon content increased from 69.06 to 94.83 wt%, while the oxygen content significantly decreased from 30.75 to 4.15 wt%. In addition, X-ray photoelectron spectroscopy (XPS) was used to

analyze the composition of LIG. The C1s profile of LIG exhibits distinct C−C peaks (Figure S7, Supporting Information). The Raman spectrum of LIG reveals three dominant peaks: the D peak at ≈1350 cm^{-1} induced by defects or bent sp^2-carbon bonds, the first-order G peak at ≈1580 cm^{-1}, and the 2D peak at ≈2700 cm^{-1}, originating from second-order zone-boundary phonons (Figure S8, Supporting Information). We also observed the surface of the fabricated LIG under various fabrication conditions (Figures S9 and S10, Supporting Information, for details of the LIG surface observation). We also measured the sheet resistance of the LIG based on the laser irradiation power and scan steps to check the electrical conductivity characteristics (Figure S11, Supporting Information, for the details of the measurements of electrical conductivity characteristics).

Figure 2b shows a schematic of the sensitive, flexible pressure sensor, where the conductive metal-deposited irregular microdome structure is used as an active layer for pressure sensing and an interdigitated electrode (IDE) based on LIG layer on a PI substrate acts as an electrode. In this study, we introduce an IDE design because its piezoresistance variation depends on the change in contact area between the microdome structure and LIG electrode. Furthermore, the irregular microdome structure enables stress concentration, leading to a heterogeneous increase in the contact area, resulting in higher sensitivity. The detailed working principle of the pressure sensor is shown in Figure 2c. In the initial state (no pressure), only a few microdome structures are in contact with the bottom LIG electrode. Given the small contact area, the conductive pathway is narrow and little current flows between the top active layer and the bottom electrodes. When the pressure is increased, additional contacts are formed between other microdome structures and the LIG electrode, resulting in a rapid decrease in resistance. The microdome structures are deformed with increasing pressure, and the contact area with the LIG electrode increases. With this irregular microdome structure, the total resistance of this sensor (R_t) can be expressed as the sum of the resistance of the metal-deposited (R_f), the resistance of the LIG electrodes (R_G), and the contact resistance between them (R_c), which can be expressed as follows

$$R_t = R_G + R_c + R_f = R_G + \cfrac{1}{\cfrac{1}{R_{C1}} + \cfrac{1}{R_{C2}} + \cdots \cfrac{1}{R_{Cn}}} + R_f \tag{1}$$

where R_{Ci} and n correspond to the contact resistance at the contact point #i and total number of electrical contacts between the top and bottom layers, respectively. As the resistance of R_G and R_f are very low owing to the high conductivity of top and bottom layers, Equation (1) can be expressed as $R_t \approx R_C$. Therefore, the change in R_c has a dominant effect on the sensing performance as the contact resistance between the microdome structures and the bottom LIG electrode changes according to the applied pressure (Figure S12, Supporting Information, for details of the equivalent circuit model).

2.3. Sensitivity of the Flexible Pressure Sensor

Figure 3 depicts the sensing performance of the flexible pressure sensor with and without an irregular microdome

structures in the pressure range of 0–400 Pa. The sensitivity S can be calculated by $S = \delta(\Delta I / I_0)/\delta p$, where ΔI, I_0, and p represent the current change, initial current, and the applied pressure, respectively. The resistive-type pressure sensor based on the composite films with 5 wt% of microspheres exhibited two different linear sensitivities under applied pressure (Figure 3a). In the first linear section up to 50 Pa, the pressure response exhibited a linear behavior and high sensitivity of 50.45 kPa^{-1}. Notably, the sensitivity of the proposed sensor (w/o microsphere expansion) is ≈85.5 times higher than that of the sensor with a smooth surface (w/o microsphere expansion). The second linear section exhibited a sensitivity of 4.35 kPa^{-1} at 50–400 Pa, which is ≈7.37 times higher than that of the sensor with a smooth surface. Previously suggested flexible pressure sensors based on regularly arranged microstructures commonly have relatively low sensitivity in the low-pressure range owing to simultaneous deformation.[11,12,23,27] However, our sensor, based on the irregular microdome structures, demonstrated excellent sensing performance in terms of sensitivity, sensing range, response time, and reliability than previously developed sensors (Figure 3b; Table S2, Supporting Information). We also checked the reproducibility by the following tests: i) size distribution of microdome structures and ii) responses of the fabricated flexible pressure sensors. The four areas of a composite film with irregular microdome structures exhibited approximately similar tendencies (Figure S13, Supporting Information). In addition, these ten different sensors exhibited similar changes in the current responses, with negligible deviations (Figure S14, Supporting Information). These results indicate that the irregular microdome structure significantly improved the sensor sensitivity in the low-pressure range while maintaining high reproducibility. Figure 3c shows the response characteristics according to the microsphere concentration with the applied pressure. Because of the microstructures, the sensor with a microsphere concentration of 5 wt% showed the highest sensitivity. At microsphere concentrations higher than 5 wt%, the composite film was bent downward for releasing compressive residual stress caused by expansion (Figure S15, Supporting Information). In addition, composite film with 5 wt% of microsphere concentration exhibited reduced mechanical properties (i.e., compressive stress and Young's modulus) for the porous effect (Figure S16, Supporting Information). Therefore, a microsphere concentration of 5 wt% was used for the additional sensor evaluation and application.

2.4. Simulation of Compressive Behavior of the Irregular Microdome Structures

FEM simulations were conducted using a representative volume element (RVE) to understand the compressive behavior of the irregular microdome structure. The RVE was generated using an FE-SEM image of the irregular microdome structure, using the following procedure. First, the center point locations and radii of each irregularly dispersed microdomes in the FE-SEM image of 200 × 250 μm^2 size were characterized using the ImageJ program (NIH, USA). Next, a realistic RVE

**ADVANCED
SCIENCE NEWS**

www.advancedsciencenews.com

**ADVANCED
FUNCTIONAL
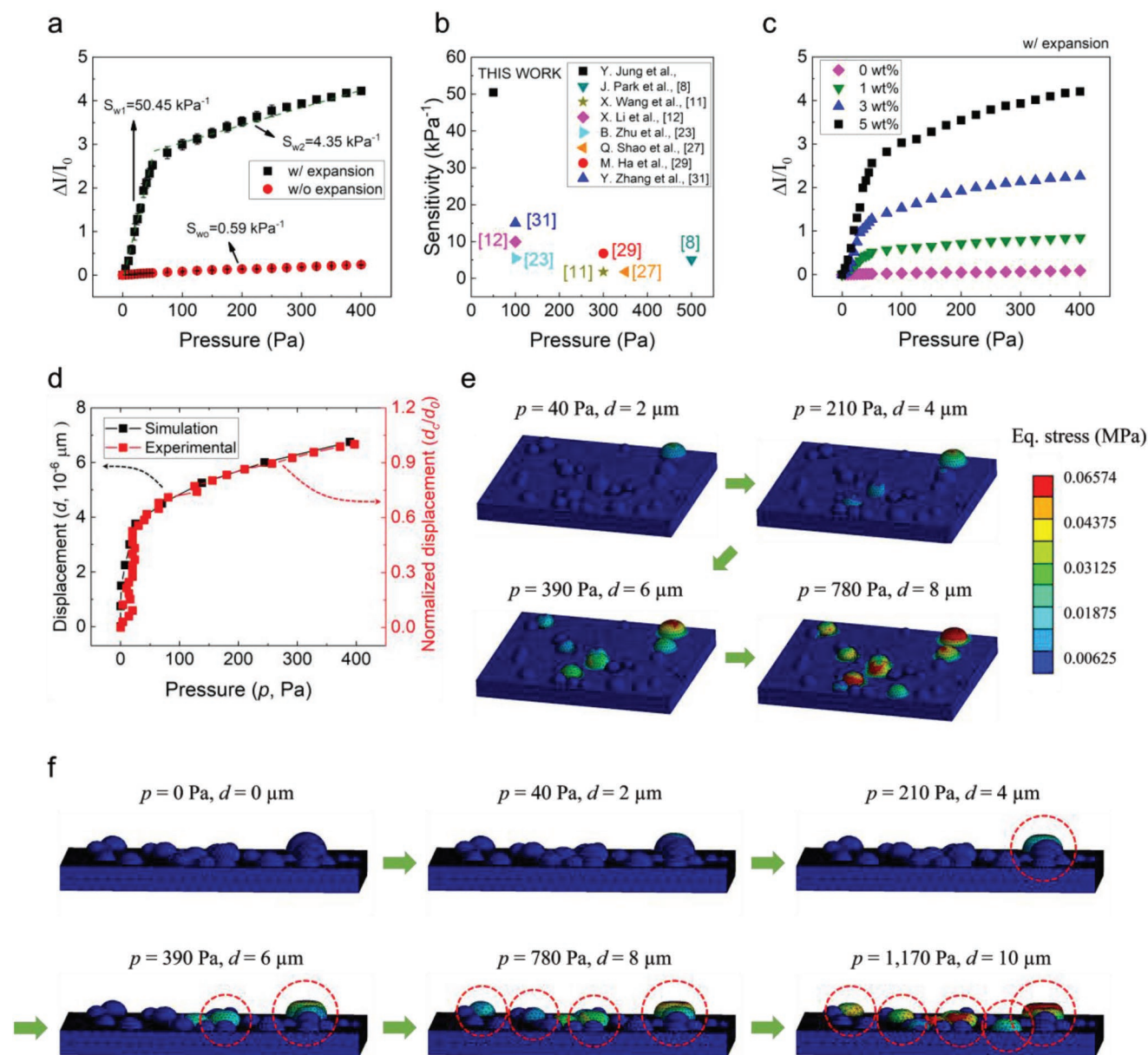MATERIALS**

www.afm-journal.de

Figure 3. Experimental and numerical analysis of the flexible pressure sensor with irregular microdome structure. a) Measured sensitivity of the flexible pressure sensor under the pressure range of 0–400 Pa. The sensitivity of the sensor based on irregular microdome structure (w/o microsphere expansion) was ≈85.5 times higher than that of the sensor with a smooth surface (w/o microsphere expansion). b) Comparison of flexible pressure sensor with previously developed pressure sensors with regular microstructures. c) Response characteristics according to the microsphere concentration with applied pressure. d) Calculated and experimental pressure–displacement curve under the pressure range of 0–400 Pa. Experimental results were normalized for comparison of tendency. The simulation results were consistent with the experimental ones. e,f) Finite-element simulation results of the local stress distribution and deformation of the irregular microdome structure under different applied pressure. The irregular microdome structures are deformed with increased pressure, and the contact area with the counter electrodes increases accordingly.

consisting of irregular microdomes having the same locations and radii of the microstructure image was reconstructed into a 3D FE simulation model (Figure S17, Supporting Information). In total, 29 microdomes were modeled in the FE simulation model. Finally, compressive deformation of the RVE via contact of the outer surface of the RVE to a flat plate was simulated using the FE method. The simulation assumed that the microspheres with a wall thickness of 0.5 μm were covered by

a 2 μm thick PDMS film near the outer surface. The microspheres and PDMS were modeled as linear elastic materials, with an elastic modulus of 500 kPa and Poisson's ratio of 0.49. We found that the simulated pressure–displacement curve from the RVE model under a pressure range of 0–400 Pa matched the experimental results very well (Figure 3d). Consistent with the experiments, the compressive displacement increased sharply with pressure until an applied pressure

of 50 Pa and then moderately increased. This pressure-displacement behavior is directly linked to the sensitivity of the pressure sensor because the larger the compressive deformation, the more the number of microdomes that are in contact between the LIG electrode. The simulation results suggest that the sharp increase in the displacement (and therefore the high sensitivity of the pressure sensor) in the pressure range of 0–50 Pa originates from the irregular microdome structure. For such a relatively low applied pressure, the contact between the irregular microdomes and the LIG electrode can occur only by a few largest microdomes, as shown by the local stress distribution of the FE model for the compressive displacement of 4 μm in Figure 3e. In this situation, the contact area increases rapidly with the applied pressure owing to the locally concentrated deformation of the few largest microdomes, thus leading to the high sensitivity of the pressure sensor. When the compressive displacement is higher than 6 μm, other smaller microdomes also make electrical contacts (Figure 3e). In addition, the microdome structures are deformed with increased pressure, and the contact area between the microdome structures and the counter electrodes is enlarged accordingly

(Figure 3f). These results suggest that the second linear section at 50–400 Pa are attributed to the wider the contact area between the irregular microdomes and the LIG electrode.

2.5. Static and Dynamic Sensing Performance of the Flexible Pressure Sensor

The sensing performance of the proposed pressure sensor was evaluated under static and dynamic pressure loadings (**Figure 4**). The relative change in the current over 5 cycles of various pressure inputs (15, 30, 45, and 60 Pa) was measured, and the repeatability results are presented in Figure 4a. We observed that our sensor exhibited stable and repeatable signals at various pressure ranges. Moreover, we examined the dynamic response characteristics of the proposed sensor. The 10% to 90% rising time (t_r) and 90% to 10% falling time (t_d) were measured as 39 and 31 ms, respectively. We also measured the subtle-pressure, as shown in Figure 4b. The current between the two electrodes of the sensors was measured in real-time, and water droplets (43 mg) were sequentially detected
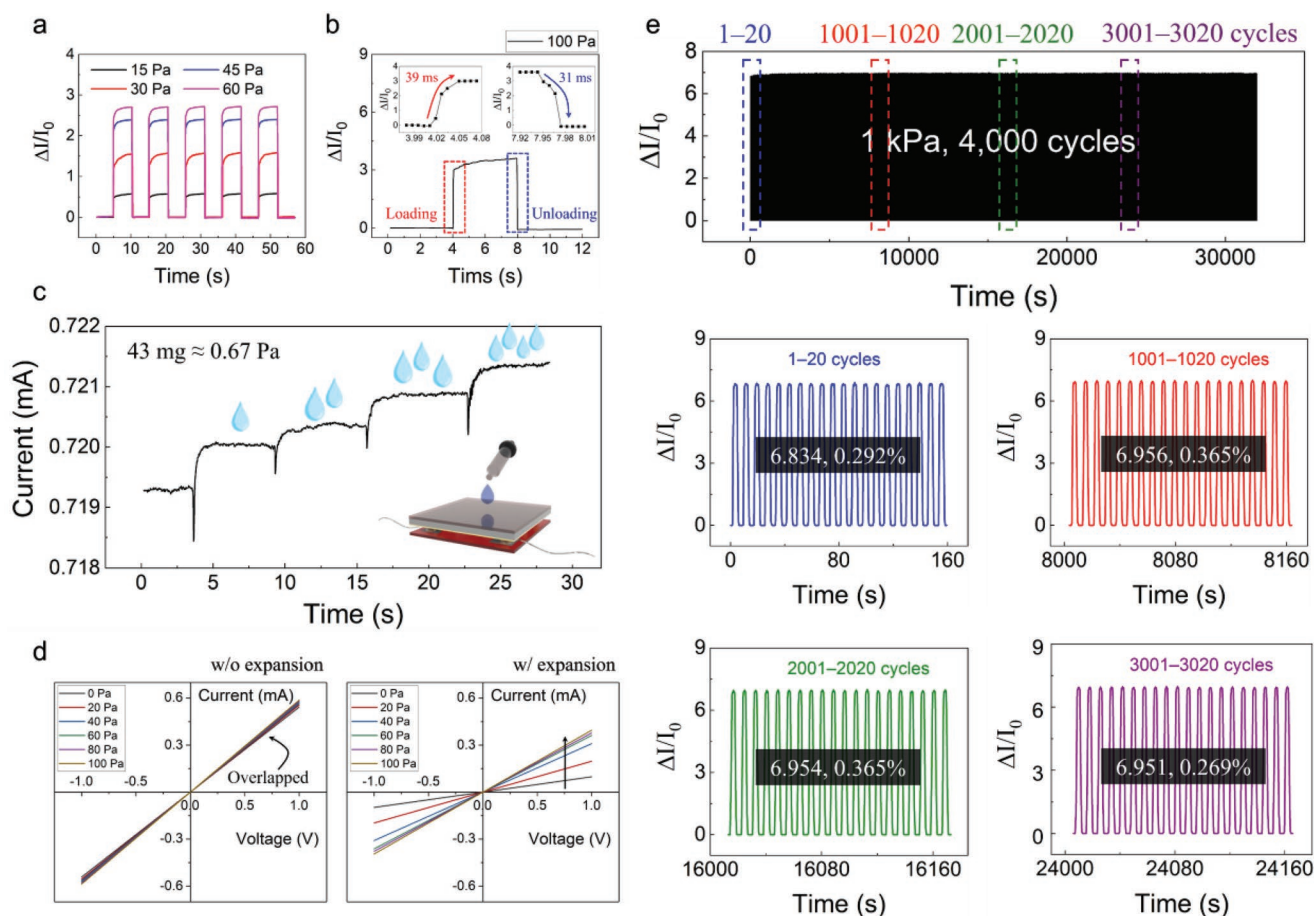

Figure 4. Analysis of the sensing performance of the pressure sensor based on irregular microdome structure under static and dynamic loading conditions. a) Repeatability test of the pressure sensor under different applied pressures. b) Response time of flexible pressure sensor to for a compressive loading of 100 Pa. The 10% to 90% rising time (t_r), and the 90% to 10% falling time (t_d) are 39 and 31 ms, respectively. c) Detection of lightweight object, i.e., water droplets of 43 mg. d) Current–voltage (I–V) characteristics of the pressure sensors with a smooth surface and irregular microdome structures. e) Reliability test by cyclic loading of 1 kPa over 4000 cycles. The blue, red, green, and purple graphs show the results of each 20 cycles (1–20, 1001–1020, 2001–2020, and 3001–3020 cycles, respectively).
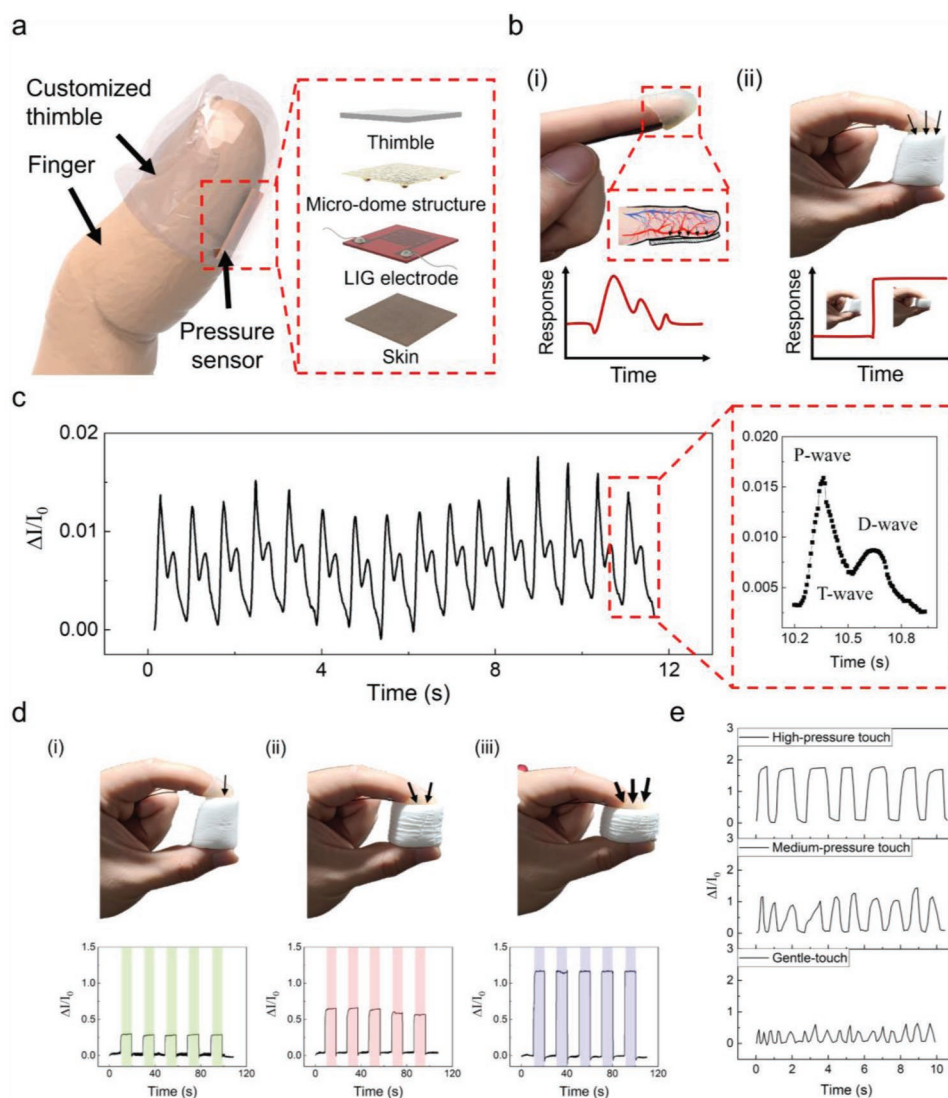
Figure 5. Demonstration of the fingertip-shaped pressure sensing with developed pressure sensor. a) Schematic illustration of the fingertip-shaped pressure sensor. b) Schematic illustration and photographs of demonstration of the blood pulse on index finger (i) and electronic skin for recognition of a soft object (ii). c) Sensor signal on the index finger. The response shows pulse waves under normal conditions (60–66 beats per minute) with typical wave shapes. d) Demonstration of the electronic skin for recognition of a soft object such as marshmallow. The sensor could accurately detect the small compressions of the soft object. e) Sensor signals with the different pressure used to touch the objects. The sensor can detect and distinguish between gentle-, medium-, and high-pressure touches.

by placing the droplets on top of the sensor (Figure 4c). The sensor exhibited a continuous response after the droplets were placed four times (Video S3, Supporting Information). We also calculated that the LOD of our sensor based on sequential detection of water droplets, as shown in Figure S18 of the Supporting Information. The theoretical LOD of our sensor was calculated as low as 0.209 Pa. To compare the sensitivity of the sensors with a smooth surface and the irregular microdome structures, we obtained the current–voltage (I–V) curves under various applied pressures (Figure 4d). When pressure was applied to the sensor with a smooth surface, the resistance hardly changed because of low sensitivity; therefore, all the I–V curves almost overlapped. By contrast, the I–V curves of the flexible pressure sensor with an irregular microdome

structures changed dramatically owing to the enhanced sensitivity. This result means that the proposed pressure sensor is sensitive enough to detect ultralow pressures, enabling applications to various target fields.

For the fabricated sensors to be used in practical applications, they must maintain stable sensing characteristics under repeated pressure loading. We evaluated the reliability of our sensor by applying repeated compression/release cycles. A pressure of 1 kPa was applied to the sensor 4000 times to investigate its long-term stability. Figure 4e presents the measurement results. Neither a shift in the sensing response nor a structural change in the sensor was observed during 4000 cycles of compression. The inset values in the middle of the graph show the average responses and standard deviations for each cycle.

In the initial 1–20 cycles, the average response was 6.834, and the standard deviation was 0.292%. Similar values were consistently measured throughout repeated compression cycles. For example, in cycles 3001–3020, the response and standard deviation were 6.951% and 0.269%, respectively. In addition, 3D profile results and FE-SEM images of composite film before and after reliability test exhibit that no significant structural distortion occurred in the microdome structure (Figure S19, Supporting Information).

2.6. Demonstration of Fingertip-Shaped Pressure Sensor

Given the excellent sensing characteristics such as high sensitivity, stability under static and dynamic applied loading, fast response, and high reliability, the proposed flexible pressure sensors are applicable for wearable devices. As one of the practical applications, we attached the sensor inside the customized thimble that perfectly fit the user's finger (**Figure 5**a). Using this fingertip-shaped pressure sensor, we demonstrated the detection of the blood pulse on the index finger and electronic skin to recognize a soft object (Figure 5b). Our sensor exhibited a high sensitivity in the low-pressure range for blood pulse detection, which is appropriate for detecting a weak signal of the blood pulse at the fingertip compared to that at the wrist. The sensor clearly detected the pulse waves under normal conditions (60–66 beats per minute) with typical wave shapes, as shown in Figure 5c (Video S4. Supporting Information). A typical carotid pulse waveform with three clear peaks was observed: the percussion wave (P-wave), tidal wave (T-wave), and diastolic wave (D-wave), which are related to the systolic and diastolic blood pressures, late systolic augmentation, and heart rate, respectively. These results suggest that the sensor can detect subtle pressures, such as the pulse at the fingertip, which indicates that it can be applied to various health monitoring fields. For the electronic skin to recognize a soft object, it is necessary to detect subtle pressure changes on the electronic skin when handling fragile/soft objects. As shown in Figure 5d, our sensor could accurately detect small compressive forces from soft objects, such as marshmallows or sponges. Moreover, the sensor can detect and distinguish between gentle-, medium-, and high-pressure touch, as shown in Figure 5e.

2.7. Demonstration of Pressure Sensor Array Pad

We present the potential applications of the proposed technology by demonstrating the pressure sensor array pad (**Figure 6**). Because the pressure sensor array pad will become one of the most important electronic devices for human–computer interaction (HCI), high performance and easy fabrication of the pressure sensor array pad are essential. Our sensor exhibits excellent sensing performance in the low-pressure range and can be readily fabricated in large-scale and complex patterns. Thus, the fabricated pressure sensor array pad can detect small changes in tactile information from the user and transmit it to the computer for various applications. In this study, we demonstrated a sensor array pad to detect a pressure distribution with 10×16 pixels. Figure 6a shows a schematic of the sensor array pad. The sensor array pad was fabricated by assembling a metal-deposited film with microdomes on the surface and LIG electrode patterns interconnected by a silver (Ag) electrode. For user convenience, the sensor array pad was covered with a soft sponge (ethylene-vinyl acetate foam). When pressure was applied to the sensor array pad, it measured the pressure applied to each pixel in real-time using an flexible printed circuit board and software. To increase the resolution and express visually from the sensor signals, we utilized a 2D/3D mapping and interpolation technique, as shown in Figure 6b. Compared to original sensor signals (Figure 6b(ii)), the interpolated sensor signals (Figure 6b(iii)) allow for the high-resolution prediction of pressure levels at adjacent locations using a limited number of sensing points. For the drawing application (Figure 6c), we drew a wave curve using a fingertip on the sensor array pad. First, we slightly pressed the sensor array pad (Figure 6c(i,ii)) and then gradually increased the pressure level while drawing a curved trajectory (Figure 6c(iii,iv)). The 2D/3D pressure mapping results show that our sensor array pad can recognize the location and sensitive pressure change during fingertip drawing (Videos S5 and S6, Supporting Information). For the multitouch application (Figure 6d), we applied pressure onto three different points of the sensor array pad with different pressure levels (gentle touch (Figure 6d(i)) and medium pressure touch (Figure 6d(ii)). From the 2D/3D mapping results, the sensor array pad successfully recognized the location and pressure levels (Video S7, Supporting Information).

After verifying the performance of the sensor array pad, we further developed a wrist-motion-based controller using deep learning (Figure 6e–h). Deep learning has been traditionally used for image processing; however, it recently has been successfully utilized in various tactile sensing applications.[33] Owing to the high sensitivity of our sensor in the low-pressure range, the sensor array pad can measure small changes in the wrist posture when the wrist is on the sensor array pad. As shown in Figure 6f, the sensor signals exhibit different patterns by different wrist movements. We used a convolutional neural network to classify four different functions: up/down/right/left movements from the sensor array pad (Figure 6g). First, the sensor signal was gathered with different wrist postures several times. Then, one hot encoding was used to provide the algorithm with the true labels. The signals (80×50 data) were put into a 1×4000 tensor. Then the output of the tensor was passed to two consecutive fully connected layers of sizes 40 and 20, respectively, with ReLU activation layers. Using this algorithm, we successfully demonstrated the control of the mouse cursor using our sensor array pad (Figure 6h; Video S8, Supporting Information).

3. Conclusion

The present study details a novel strategy to generate 3D and irregular microdome structures with microspheres that expand at a specific temperature. By mixing microspheres and elastomer and applying a heat expansion treatment, we could fabricate large-area, flexible, and irregular microdome structures without the need for any micropattern mold. A composite film with an irregular microdome structure was applied to the
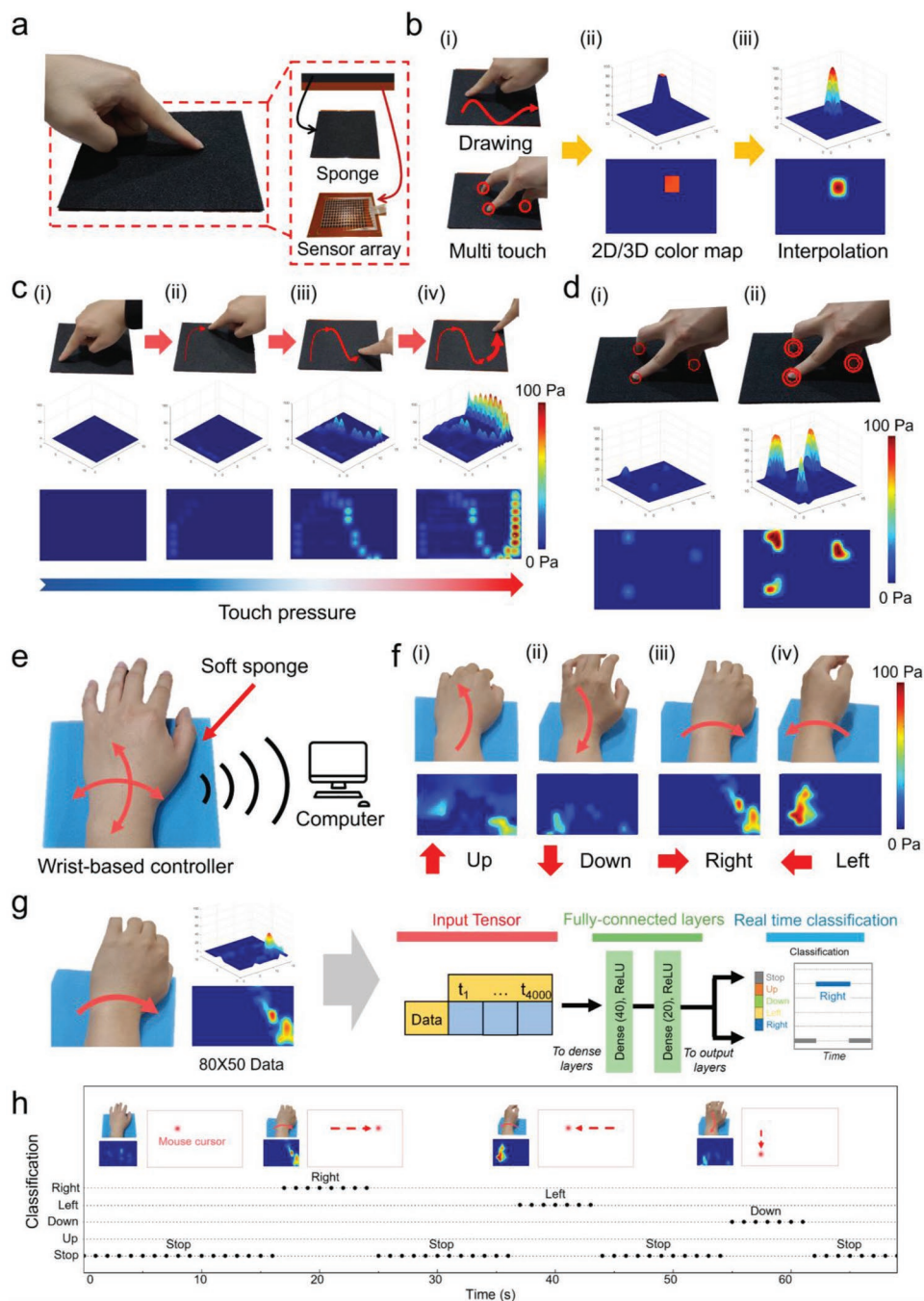
Figure 6. Demonstration of pressure sensor array pad with 10×16 pixels for human computer interaction. a) Photographs of demonstration of the pressure sensor array pad. The sensor array pad was fabricated through assembling metal deposited irregular microdome structures, LIG patterned electrodes, and the soft sponge. b) Illustration of signal processing of the pressure sensor array pad. When pressure is applied to the sensor array pad, pressure at each pixel is measured in real time (i), using 2D/3D mapping and interpolation technique (ii, iii). c) Demonstration of the drawing application. At first, we slightly pressed the sensor array pad (i, ii), and then increased pressure level gradually (iii, iv) while drawing a curved trajectory. d) Demonstration of the multi touch application. Applying pressure onto three different points of the sensor array pad with different pressure levels (gentle touch (i) and medium pressure touch (ii)). e) Photographs of demonstration of wrist motion-based controller using deep learning. f) Sensor signals with different patterns with different wrist movements (up (i), down (ii), right (iii), and left (iv)). g) Deep learning process for real time classification of four different functions such as up/down/right/left movements from the sensor array pad. h) Result of deep learning process for classification of movements and control of the mouse cursor.

sensing film of a high-performance pressure sensor, simultaneously featuring high sensitivity and flexibility. The proposed flexible pressure sensor based on an irregular microdome structure exhibited much higher sensitivity than previously suggested sensors based on regular microstructures. Through FEM simulations and experiments, we confirmed that the sensitivity

enhancement of the pressure sensor originates from the heterogeneous contact change between the irregular microdome structures and LIG electrodes. In addition, the sensor showed a fast response time ($\tau_{10-90\%} \approx 39$ ms), excellent repeatability, and high reliability. The flexible pressure sensor was successfully utilized in a fingertip-shaped pressure sensor to monitor subtle pulse signals at the index finger and to recognize soft objects in real-time. Finally, to demonstrate the large-area application of the proposed pressure sensor, a multipixel sensor pad was fabricated and evaluated for HCI applications. As a result, we confirmed that the suggested 3D surface morphology via internal popping of microspheres could be applied in pressure sensors with high performance in terms of sensitivity, flexibility, scalability, and reliability. We believe that the present study opens a new avenue for the fabrication of 3D surface morphology for highly sensitive pressure sensors with excellent sensing performance. We expect that our study will provide a new route toward advanced pressure sensors for promising applications including human–machine interfaces, health-monitoring systems, interactive robot control, etc.

4. Experimental Section

Fabrication of the Composite Films with 3D Surface Morphology: First, thermally expandable microspheres (Microsphere, MSH-320, SDI Korea, Korea) were added to the well-mixed liquid PDMS precursor (Sylgard 184, Dow Corning Corporation, USA), in which the resin and hardener were mixed in a 10:1 weight ratio. For uniform mixing and degassing, the PDMS/microsphere precursor was mixed for 90 s in a 7:6 revolution-rotation ratio using a planetary mixer (KK-V350W, KURABO, Japan). The thickness of the spin-coated composite film with microsphere affects the surface morphology, the PDMS/microsphere precursor was spin-coated on the PI substrate at 1000 rpm for 30 s to control the thickness of the composite film as ≈110 µm (Figure S20, Supporting Information). And then the composite film cured at 80 °C for 4 h. To maximize the microsphere expansion, the fully cured composite film was heated at 170 °C for 5 min. Metal deposition (Ti/Au 10/30 nm) was conducted by sputtering on the surface with irregular microdomes to form a uniform conductive layer. Second, a commercial PI film (PI film, Young Woo Trading, Korea) with a thickness of 75 µm was cleaned and prepared. The LIG was grown directly on a PI substrate using CO_2 laser equipment (C30, Coryart, Korea). The scanning power and interval between the scan steps were 30% of the maximum power (40 W) and 0.075 mm, respectively. Sensing lines were connected to both pads on the IDE using a silver epoxy (CW-2400, ITW Chemtronics, USA).

Characterization of the Composite Films with Irregular Microdome Structure and Flexible Pressure Sensor: Real-time images of microspheres during expansion were obtained using an optical microscope (VHX-500F, KEYENCE, Japan). The morphologies of the composite film and LIG were characterized using FE-SEM (Supra 40VP, Carl Zeiss NTS GmbH, Oberkochen, Germany). A 3D laser scanning confocal microscope (VX-X1050, KETENCE, Japan) was used to measure the 3D surface morphology. Surface roughness measurements were performed using a portable surface roughness tester (SJ-210, MITUTOYO, Japan) with a scan length of 4 mm. The chemical composition of the composite structure was analyzed from the C1s spectrum obtained via XPS (Axis Supra, Kratos Analytical Limited (Shimadzu), Manchester, UK). A four-point probe (CMT-SR2000N, Advanced Instrument Technology, Korea) was used to measure the sheet resistance of the LIG, and the average and deviation were calculated by measuring 50 points for each condition. To verify the sensing performance, a high-precision universal testing machine (UTM)(AGS-X (1 kN), Shimadzu Corporation, Japan) equipped with a load cell (maximum load = 1000 N) was used. A disk

with a diameter of 50 mm was used to apply a uniform pressure to the sensor. The response of the sensor was measured using a parameter analyzer (Keithley 4200 SCS, Tektronix, USA). The UTM was employed to compress the composite film at 0.8 mm displacement (10% strain). The composite film was compressed at a speed of 1 mm min^{-1}, and had a diameter of 30 mm and thickness of 8 mm.

Fabrication of the Fingertip-Based Pressure Sensor: A fingertip-based pressure sensor was fabricated using the following sequential steps. First, Alja Safe powder (SmoothOn, USA) was mixed with water to form a rubbery elastomer, which was subsequently poured into a container. Second, the target user's finger was dipped into the container for 5 min until it was cured to form a mold for the customized thimble. Third, Ecoflex00-35 (Smooth-On, USA) was poured into the mold back and forth to form a customized thimble. Finally, the sensor was placed in the thimble and then covered with a thin Ecoflex00-35 (Figure S21, Supporting Information). The output from the sensor was measured using a source meter (Keithley 2400, Tektronix, USA). This experiment was approved by the institutional review board (IRB) of Korea Advanced Institute of Science and Technology (KAIST) (IRB No. KH2021-151). All participants provided written, informed consent prior to participation in this study.

Fabrication of the Pressure Sensor Array Pad: The pressure sensor array pad was fabricated by the following sequential steps. First, a shadow mask was mounted onto composite films with irregular microdomes on the surface. Second, a metal layer (Ti = 10 nm, Au = 30 nm) was deposited using sputtering process. Third, the LIG electrode was fabricated using patterned LIG with 10×16 pixels and screen printing with Ag ink (Figures S22 and S23, Supporting Information). Finally, the sensor array pad was fabricated by assembling the composite film and LIG arrays with a covering sponge (Figure S24, Supporting Information). Subsequently, this pressure sensor array was connected to the microcontroller (Teensy, PJRC, USA) to measure the resistance. Using software programs such as MALAB (MathWorks, USA) and Jupyter Notebook (Jupyter, USA), 2D/3D visualization and deep learning were conducted. Regarding the deep learning process, the sensor signal was gathered several times. Then, one hot encoding was used to provide the algorithm with the true labels. The signals (80×50 data) were put into a 1×4000 tensor. Then the output of the tensor was passed to two consecutive fully connected layers of sizes 40 and 20, respectively, with ReLU activation layers.

Supporting Information

Supporting Information is available from the Wiley Online Library or from the author.

Conflict of Interest

The authors declare no conflict of interest.

Author Contributions

Y.J. and J.C. contributed equally to this work. The manuscript was written through contributions of all authors. All authors have given approval to the final version of the manuscript.

[1] X. Wang, L. Dong, H. Zhang, R. Yu, C. Pan, Z. L. Wang, *Adv. Sci.* **2015**, *2*, 1500169.

[2] S. Jung, J. H. Kim, J. Kim, S. Choi, J. Lee, I. Park, T. Hyeon, D. H. Kim, *Adv. Mater.* **2014**, *26*, 4825.

[3] M. Zhong, L. Zhang, X. Liu, Y. Zhou, M. Zhang, Y. Wang, L. Yang, D. Wei, *Chem. Eng. J.* **2021**, *412*, 128649.

[4] W. Honda, S. Harada, T. Arie, S. Akita, K. Takei, *Adv. Funct. Mater.* **2014**, *24*, 3299.

[5] T. Gong, H. Zhang, W. Huang, L. Mao, Y. Ke, M. Gao, B. Yu, *Carbon* **2018**, *140*, 286.

[6] K. Kim, J. Choi, Y. Jeong, I. Cho, M. Kim, S. Kim, Y. Oh, I. Park, *Adv. Healthcare Mater.* **2019**, *8*, 1900978.

[7] Y. Jung, K. K. Jung, D. H. Kim, D. H. Kim, J. S. Ko, *Polymers* **2020**, *12*, 1499.

[8] J. Park, Y. Lee, J. Hong, M. Ha, Y. D. Do Jung, H. Lim, S. Y. Kim, H. Ko, *ACS Nano* **2014**, *8*, 4689.

[9] L. Pan, A. Chortos, G. Yu, Y. Wang, S. Isaacson, R. Allen, Y. Shi, R. Dauskardt, Z. Bao, *Nat. Commun.* **2014**, *5*, 3002.

[10] Y. Jung, K. K. Jung, D. H. Kim, D. H. Kwak, S. Ahn, J. S. Han, J. S. Ko, *Sens. Actuators, A* **2021**, *331*, 113034.

[11] X. Wang, Y. Gu, Z. X., Z. Cui, T. Zhang, *Adv. Mater.* **2013**, *26*, 1336.

[12] X. Li, W. Huang, G. Yao, M. Gao, X. Wei, Z. Liu, H. Zhang, T. Gong, B. Yu, *Scr. Mater.* **2017**, *129*, 61.

[13] O. Atalay, A. Atalay, J. Gafford, C. Walsh, *Adv. Mater. Technol.* **2018**, *3*, 1700237.

[14] S. C. B. Mannsfeld, B. C. K. Tee, R. M. Stoltenberg, C. V. H. H. Chen, S. Barman, B. V. O. Muir, A. N. Sokolov, C. Reese, Z. Bao, *Nat. Mater.* **2010**, *9*, 859.

[15] Y. Jung, T. Lee, J. Oh, B. G. Park, J. S. Ko, H. Kim, J. P. Yun, H. Cho, *ACS Appl. Mater. Interfaces* **2021**, *13*, 28975.

[16] B. C.-K. Tee, A. Chortos, R. R. Dunn, G. Schwartz, E. Eason, Z. Bao, *Adv. Funct. Mater.* **2014**, *24*, 5427.

[17] J. Choi, D. Kwon, K. Kim, J. Park, D. D. Orbe, J. Gu, J. Ahn, I. Cho, Y. Jeong, Y. S. Oh, I. Park, *ACS Appl. Mater. Interfaces* **2020**, *12*, 1698.

[18] Q. Gao, H. Meguro, S. Okamoto, M. Kimura, *Langmuir* **2012**, *28*, 17593.

[19] Y. Hu, C. Xu, Y. Zhang, L. Lin, R. L. Snyder, Z. L. Wang, *Adv. Mater.* **2011**, *23*, 4068.

[20] K. Y. Lee, H. J. Yoon, T. Jiang, X. Wen, W. Seung, S. W. Kim, Z. L. Wang, *Adv. Energy Mater.* **2016**, *6*, 1502566.

[21] J. H. Lee, H. J. Yoon, T. Y. Kim, M. K. Gupta, J. H. Lee, W. Seung, H. Ryu, S. W. Kim, *Adv. Funct. Mater.* **2015**, *25*, 3203.

[22] J. Choi, D. Kwon, B. Kim, K. Kang, J. Gu, J. Jo, K. Na, J. Ahn, D. Del Orbe, K. Kim, J. Park, J. Shim, J. Y. Lee, I. Park, *Nano Energy* **2020**, *74*, 104749.

[23] B. Zhu, Z. Niu, H. Wang, W. R. Leow, H. Wang, Y. Li, L. Zheng, J. Wei, F. Huo, X. Chen, *Small* **2014**, *10*, 3625.

[24] Y. Xiong, Y. Shen, L. Tian, Y. Hu, P. Zhu, R. Sun, C.-P. Wong, *Nano Energy* **2019**, *70*, 104436.

[25] Y. Zhang, F. Han, Y. Hu, Y. Xiong, H. Gu, G. Zhang, P. Zhu, R. Sun, C.-P. Wong, *Macromol. Chem. Phys.* **2020**, *221*, 2000073.

[26] H. Wang, Y. Cen, X. Zeng, *ACS Appl. Mater. Interfaces* **2021**, *13*, 28538.

[27] Q. Shao, Z. Niu, M. Hirtz, L. Jiang, Y. Liu, Z. Wang, X. Chen, *Small* **2014**, *10*, 1466.

[28] H. Park, Y. R. Jeong, J. Yun, S. Y. Hong, S. Jin, S. J. Lee, G. Zi, J. S. Ha, *ACS Nano* **2015**, *9*, 9974.

[29] M. Ha, S. Lim, J. Park, D.- S. Um, Y. Lee, H. Ko, *Adv. Funct. Mater.* **2015**, *25*, 2841.

[30] S. Peng, P. Blanloeuil, S. Wu, C. H. Wang, *Adv. Mater. Interfaces* **2018**, *5*, 1800403.

[31] Y. Zhang, Y. Hu, P. Zhu, E. Han, F. Han, Y. Zhu, R. Sun, C.-P. Wong, *Adv. Mater. Interfaces* **2017**, *9*, 35968.

[32] J. Lin, Z. Peng, Y. Liu, F. Ruiz-Zepeda, R. Ye, E. L. G. Samuel, M. J. Yacaman, B. I. Yakobson, J. M. Tour, *Nat. Commun.* **2014**, *5*, 5.

[33] S. Chun, J.-S. Kim, Y. Yoo, Y. Choi, S. J. Jung, D. Jang, G. Lee, K.-I. Song, K. S. Nam, I. Youn, D. Son, C. Pang, Y. Jeong, H. Jung, Y.-J. Kim, B.-D. Choi, J. Kim, S.-P. Kim, W. Park, S. Park, *Nat. Electron.* **2021**, *4*, 429.